Micro-CT and Histological Evaluation of an Neural Interface Implanted Within a Blood Vessel

Nicholas Lachlan Opie*, Nicole R. van der Nagel, Sam E. John, Kirstan Vessey, Gil S. Rind, Stephen M. Ronayne, Erica L. Fletcher, Clive N. May, Terence J. O'Brien, and Thomas J. Oxley

Abstract*—*Objective: **Recently, we reported the development of a stent-mounted electrode array (Stentrode) capable of chronically recording neural signals from within a blood vessel with high fidelity. Preliminary data suggested incorporation of the Stentrode into the blood vessel wall was associated with improved recording sensitivity. We now investigate neointimal incorporation of the Stentrode, implanted in a cohort of sheep for up to 190 days.** ***Methods:*** **Micro-CT, obtained from the Imaging and Medical Beamline at the Australian Synchrotron, and histomorphometic techniques developed specifically for evaluation of cerebral vasculature implanted with a stent-electrode array were compared as measures to assess device incorporation and vessel patency.** ***Results:*** **Both micro-CT analysis and histomorphometry, revealed a strong correlation between implant duration and the number of incorporated stent struts. <10% (26/268) of stent struts were covered in neointima in sheep implanted for <2 weeks, increasing to >78% (191/243) between 2 and 4 weeks. Average strut-to-lumen thickness from animals implanted >12 weeks was comparable across both modalities, $339 \pm 15\,\mu\mathrm{m}$ measured using micro-CT and $331 \pm 19\,\mu\mathrm{m}$ ($n = 292$) measured histologically. There was a strong correlation between lumen areas measured using the two modalities ($p < 0.001$), with no observation of vessel occlusion observed from any of the 12 animals implanted for up to 190 days.** ***Conclusion:*** **Micro-CT and the histomorphometric techniques we developed are comparable and can both be used to identify incorporation of a Stentrode implanted in cerebral vessels.** ***Significance:*** **This study demonstrates preliminary safety of a stent-electrode array implanted in cerebral vasculature, which may facilitate technological advances in minimally invasive brain–computer interfaces.**

***Index Terms*—Brain–computer interface, endovascular stent-electrode array, histology, neuroimaging, synchrotron.**

I. Introduction

RECENT years have seen an increase in the use of neural implants for chronic recording and stimulation in the diagnosis, rehabilitation, and treatment of patients with epilepsy, paralysis, and a range of neuropsychiatric disorders [1]–[3]. Despite the wide ranging use of chronic neural implants, the functionality of these devices is often impeded by biotic and abiotic responses. Breach of the blood–brain barrier induces gliosis and immunological responses which can cause electrode decomposition and failure [4]–[9]. Due to these shortcomings, there has been an increasing interest in developing neural interfaces that are optimized for chronic implantation. One option to reduce risks associated with infection and device rejection is to implant chronic electrode arrays inside cerebral blood vessels, removing the requirement for craniotomy, which may be associated with significant morbidity [10]. Previous work has demonstrated the capacity of electrode arrays implanted within cerebral blood vessels to record high fidelity neural information for durations greater than 190 days [11]. By providing minimally invasive access to regions of superficial cortex, endovascular neural interface technology could be used to detect epileptic seizures or to enable direct brain control of prosthetic limbs, computers, wheelchairs, and exoskeletons by patients with a paralyzing spinal cord lesion or limb amputation.

To secure electrodes and ensure vessel patency is maintained, endovascular electrode arrays can be mounted on self-expanding Nitinol stents. However, there is a risk that metal from the stent may cause a thrombus to develop [12]. When a stent is implanted in a vessel, the inner intimal layer of the vessel grows over the stent struts, incorporating them into the vessel wall. This is thought to reduce the likelihood of thrombosis [13], [14]. Mesh-like stents, designed to reduce the volume of implanted material, also retain a pathway for transmission of fluids and chemicals through the vessel wall that acts to further improve the stent strut coverage by endothelial cell layers.

Manuscript received January 14, 2016; revised February 24, 2016; accepted April 5, 2016. Date of publication June 21, 2016; date of current version March 17, 2017. This work was supported by Defense Advanced Research Projects Agency MTO Contract No. N66001-12-1-4045; Office of Naval Research Global No. N62909-14-1-N020; National Health and Medical Research Council of Australia Project Grant APP1062532 and Development Grant APP1075117. This research was undertaken, in part, on the Medical Imaging Beamline at the Australian Synchrotron, VIC, Australia. *Asterisk indicates corresponding author.*

*N. L. Opie is with the Vascular Bionics Laboratory, The Department of Medicine, The University of Melbourne, Melbourne, VIC 3010, Australia, with The Florey Institute of Neuroscience and Mental Health, The University of Melbourne, Parkville, VIC 3052, Australia, and also with the Department of Electrical and Electronic Engineering, The University of Melbourne, Parkville, VIC 3010, Australia (e-mail: nicholas.opie@unimelb.edu.au).

N. R. van der Nagel, G. S. Rind, S. M. Ronayne, C. N. May, T. J. O'Brien, and T. J. Oxley are with the Vascular Bionics Laboratory, The Department of Medicine, The University of Melbourne, and also with The Florey Institute of Neuroscience and Mental Health, The University of Melbourne.

E. L. Fletcher and K. Vessey are with the Department of Anatomy and Neuroscience, The University of Melbourne.

S. E. John is with the Vascular Bionics Laboratory, The Department of Medicine, The University of Melbourne, with The Florey Institute of Neuroscience and Mental Health, The University of Melbourne, and also with the Department of Electrical and Electronic Engineering, The University of Melbourne.

Digital Object Identifier 10.1109/TBME.2016.2552226

A common phenomenon that has been observed in implanted stents, particularly bare metal stents, is in-stent restenosis, which has been a problem for interventional cardiology [15] and endovascular surgery [16]. Neointimal proliferation, a cause of in-stent restenosis, is associated with medial smooth muscle cell migration and the production of a vascular extracellular matrix that narrows the lumen, resulting in the stent no longer being effective at maintaining vessel patency [17]. Though the characterization of neointimal proliferation in stented coronary vessels is well documented [18]–[20], there are few reports with respect to neointimal proliferation in stented cerebral veins [21]. In work by Wright *et al.* [22], it was suggested that venous stents may be more quickly incorporated into the vessel than arterial stents.

In recent work, we demonstrated the capacity of using synchrotron radiation to obtain high resolution, nondestructive micro-CT images of animals implanted with a Stentrode. The clear visualization of the internal lumen enabled assessment of vessel patency, however, there have been some reports suggesting that metallic artifacts such as blooming and streaking can lead to artificial measurements of lumen diameter [23], [24]. As a result, it is necessary to investigate, develop, and compare histological methods of assessing neointimal incorporation with micro-CT measurements. We present here the first analysis of stent neointimal growth within a cerebral venous sinus relating to a stent-based electrode array.

II. Materials and Methods

A. Stentrode Fabrication and Surgical Procedure

Fabrication of the Stentrode and surgical procedures have been described previously [11]. Briefly, Stentrodes were fabricated by mounting 750 μm diameter and 50-μm-thick laser cut platinum disc electrodes onto commercially available stent (Solitaire SAB; Covidien, CA, USA). 30-mm-long self-expanding Nitinol stents with a 3-mm expanded diameter and strut thickness between 50 and 70 μm [25] were used in these experiments. A 250-μm-diameter polytetrafluoroethylene-coated guide wire (Separator 032, Penumbra, CA, USA) was attached to the stent using ultraviolet curable adhesive (Dymax 1128-A-M, UV Pacific) to assist with deployment. The 25-μm-diameter polyimide-coated platinum–tungsten (92%/8%) leadwires (Goodfellow) were welded to the electrodes and wrapped around the stent struts and along the guide wire for attachment to external equipment.

In this paper, 12 adult (2–4 years) Corriedale ewes weighing 40–70 kg were used. Experiments were conducted at The Florey Institute of Neuroscience and Mental Health and were approved by the Howard Florey Animal Ethics Committee. Experiments were in accordance with the NH&MRC Principles of laboratory animal care, Prevention of Cruelty to Animals Act, Australia, 2004 and the NHMRC Australian Code of Practice for the Care & Use of Animals for Scientific Purpose (seventh edition, 2004). For all sheep, devices were inserted via a cut-down and direct cannulation of the jugular vein followed by advancement into the superior sagittal sinus, which overlies the motor cortex (see Fig. 1), under visual guidance using digital subtraction angiography with roadmapping (Arcadis Avantic, Siemens, Munich, Germany). Device position was assessed immediately postdeployment, on completion of the surgery and, in a small cohort of animals, at one and three months following implantation, with no device movement or positional change observed.

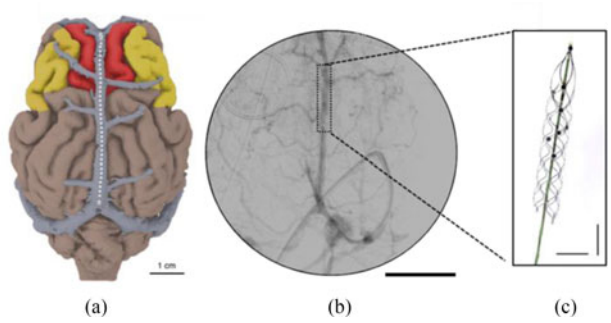

Fig. 1. (a) Three-dimensional reconstruction of the sheep brain showing the superior sagittal sinus (SSS) overlying the motor cortex (red) and sensory cortex (yellow). (b) Venogram of sheep implanted with a Stentrode in the SSS. Scale bar, 20 mm. (c) Stentrode showing electrodes mounted on a self-expanding stent. Scale bar, 5 mm.

Animals were administered antiplatelet medication daily from two days prior to implantation to minimize thrombosis (Aspirin, 100 mg). In addition, animals were given a heparin bolus (150 units per kg) during the surgical procedure to prevent acute thrombus formation. Animals were observed for up to 190 days, after which the sheep were euthanized through lethal injection of sodium pentobarbitone. Brain tissue and vessel fixation was performed with bilateral carotid arterial infusion of saline followed by 10% formaldehyde.

B. Synchrotron Imaging and Analysis

Prior to evaluation and imaging of tissue using the Australian Synchrotron, tissues were immersed in Lugol's solution (5% wt/v iodine, 10% wt/v potassium iodine; Complementary Components, Australia) for 96 h [26]. Images were acquired at the Imaging and Medical beamline of the 3.0 GeV Australian Synchrotron with a 136 m source-to-sample distance. Samples were scanned at 50 KeV using a Ruby detector (4Dx, Melbourne, Australia) with a 25-μm-thick scintillator and sample-to-detector distance of 1000 mm (0.4 s exposure). A total of 1800 high-resolution images (13.75 μm pixels) were taken as the sample was rotated around 180°, with an additional 20 dark and light-field frames taken for image correction [27]. Images were reconstructed using XTRACT (MASSIVE CWSx64, Version 8.1.2.6829M, CSIRO, Australia) to form sequential z-stacks, which were imported into ImageJ (1.48i, NIH, USA) for analysis.

Stentrode incorporation into vessel wall was quantified by measuring strut-to-lumen distances, taken at sections between electrodes along the Stentrode length to avoid artifacts caused by the reflective platinum electrodes. To minimize the error relating to blooming artifact of the stent struts, strut-to-lumen measurements (see Fig. 2) were taken from the center of the strut [28]. Lumen area was defined as a congruent area of reduced density with respect to the surrounding vessel wall and dura, and was measured using digital morphometry from a minimum of slices taken at 1 mm intervals from the distal to proximal ends of the Stentrode.

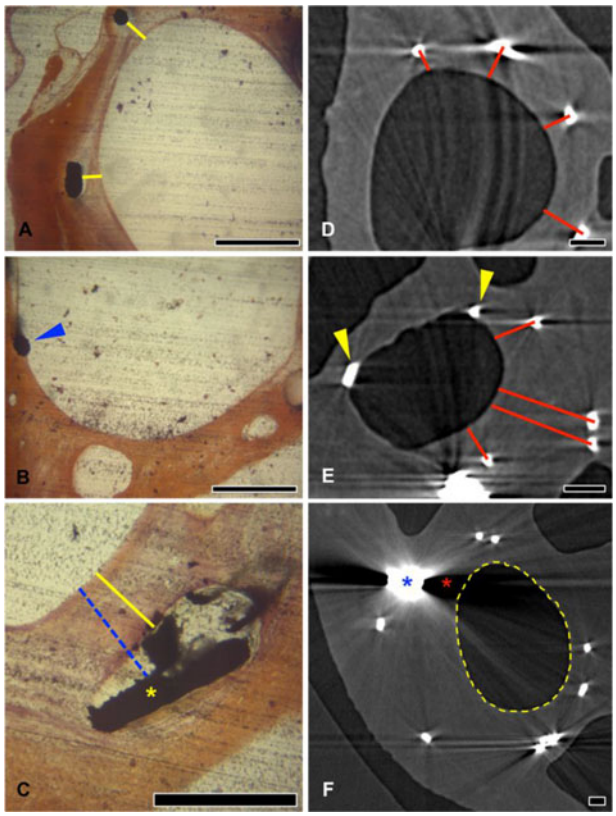

Fig. 2. Morphometric analysis of device intimal incorporation. Histological evaluation of neointimal thickness samples embedded in an epoxy resin and stained with haematoxylin, showing (A) measurement of strut-to-lumen distance (yellow lines) measured from the internal edge of the stent strut to the nearest point of the internal lumen, (B) a strut deemed to be uncovered (or minimally covered) by neointima (blue arrowhead), and (C) an implanted electrode (yellow asterisk) showing the recorded thickness of the neointima growing over the electrode, wire, and material used for electrode adhesion (yellow line). Measurements from the electrode to lumen (blue dotted line) were not used to calculate neointimal thickness due to variability in the amount of adhesive used to secure the electrodes and lead wires to the stent. (D)–(F): High-resolution micro-CT evaluation of implanted devices from tissue pre-immersed in iodine and scanned using the Australian Synchrotron Imaging and Medical beamline, showing (D) the strut-to-lumen distance, measured from the center of each strut to the nearest internal lumen edge (red lines) to reduce any blooming artifact variability, (E) two struts deemed to be uncovered or minimally covered (yellow arrowheads), (F) the electrode (blue asterisk) experiences a significant blooming artifact. It is not possible to determine the true edge of the electrode, and a dark artifact (red asterisk) obscures the assumed lumen boundary (yellow dotted line); therefore, electrode-to-lumen distance could not be faithfully measured using micro-CT. Scale bar, 500 μm.

C. Histopathology and Histomorphometry

Following synchrotron imaging, samples were dissected to remove excess tissue surrounding the superior sagittal sinus and implanted electrode array. Samples, measuring approximately $5\,\mathrm{mm} \times 5\,\mathrm{mm} \times 30\,\mathrm{mm}$, were then twice washed in 1 M phosphate-buffered saline for 10 min and dehydrated using increasing concentrations of methanol (70%, 80%, and 90% methanol solutions) for 1 h each. Samples were then twice washed in 100% methanol and twice immersed in 100% acetone for 2 h each. The tissue was then infiltrated using 75% epoxy resin (DDSA; ProSciTech, QLD, Australia) and 25% acetone overnight on a rotating platform. Samples were infiltrated with 100% resin for 6 h at room temperature prior to curing overnight at 70 °C–75 °C. To enable sectioning of samples containing both tissue and metal, a modified protocol was devised based on the saw–grinder methods reported by Malik *et al*. and Rippstein *et al*. [29], [30], using an Accutom-50 saw/grinder machine (Struers; Denmark) that was fitted with a $152\,\mathrm{mm} \times 0.4\,\mathrm{mm} \times 12.7\,\mathrm{mm}$ diamond cutoff wheel. Each resin embedded specimen yielded 13 ± 4 sections, with 200–800 μm thick slices taken at 1–1.5 mm intervals. Samples were then sanded to reduce sample skewing that could produce an artificially lengthened section. The average section thickness produced was $472 \pm 185\,\mu\mathrm{m}$ (mean $\pm$ SD). The kerf loss of sample material that occurred due to the thickness of the blade was approximately 600–800 μm per section. Each section was then mounted to a glass slide (Ward's petrographic microscope slide; Rochester, NY, USA) using cyanoacrylate (Loctite glass glue; Henkel, Germany). Harris' haematoxylin (American MasterTech, USA) was then applied directly to the resin-embedded tissue sections for 36 h at 37 °C without prior deplasticization. It was observed that eosin greatly overstained the tissue and the resin and was excluded. Images of the stained samples were captured using a Laborlux D light microscope (Leitz, Germany) at 4$\times$ magnification, fitted with a Leica DFC320 camera (Germany) and Leica Application Suite V4.2 software. The digital photographs were imported into ImageJ (1.48V, NIH, USA) and the distance from the edge of each device strut and electrode to the nearest vessel lumen edge was measured. Strut-to-lumen distances and the proportion of struts that were observed to be completely covered in intima were also measured.

D. Statistical Analysis

Animals were grouped into subsets based on the duration of implantation, with two animals in each of the 0 to 2 week (0, 9 days), 2 to 4 week (14, 27 days), and 4 to 8 week (34, 56 days) subgroups. Three animals were implanted for each of the 8 and 12 week (77, 83, and 98 days) and 12 to 24 week (124, 153, and 190 days) subgroups. Three nonimplanted controls were also assessed. A two-tailed Pearson correlation was computed between micro-CT images and histological sections for percentage of incorporated struts, strut-to-lumen distance, and lumen area, with $\alpha = 0.05$. All analysis was randomized and performed by blinded assessors.

III. Results

A. Stent Strut Intimal Incorporation

Micro-CT and histological techniques were used to evaluate neointimal proliferation occurring in 12 animals implanted with a Stentrode in the superior sagittal sinus for up to 190 days. Using both techniques, we analyzed the number of stent struts covered in neointima as a function of implant duration and calculated the average distance between the stent struts and the internal lumen (see Table I). There was a significant increase in the percentage of incorporated struts as implant durations increased beyond 2 weeks for both the micro-CT and histologically assessed samples (see Fig. 3). As measured by micro-CT,

TABLE I

MICRO-CT AND HISTOPATHOLOGICAL MEASUREMENTS FROM 12 ANIMALS IMPLANTED WITH A STENT-MOUNTED ELECTRODE ARRAY IN THE SUPERIOR SAGITTAL SINUS FOR UP TO 190 DAYS INDICATING THE NUMBER OF STRUTS INCORPORATED, THE NUMBER OF STRUTS THAT WERE NOT COVERED IN NEOINTIMA AND THE PERCENTAGE OF INCORPORATED STRUTS

Duration Subset	Duration of Implantation	Strut Coverage (Struts Covered/Total Struts (%))		Strut-to-Lumen Distance (μm, mean $\pm$ SEM)	
		Micro-CT	Histopathology	Micro-CT	Histopathology
0–2w	0	8/35 (22.9%)	4/100 (4.00%)	–	–
	9	8/49 (16.3%)	6/84 (7.14%)	–	–
2–4w	14	58/69 (84.1%)	68/78 (87.2%)	597 $\pm$ 46	222 $\pm$ 28
	27	47/76 (61.8%)	18/20 (90.0%)	536 $\pm$ 48	376 $\pm$ 54
4–8w	34	34/47 (72.3%)	67/78 (85.9%)	346 $\pm$ 37	213 $\pm$ 26
	56	71/82 (86.6%)	87/91 (95.6%)	322 $\pm$ 22	231 $\pm$ 24
8–12w	77	106/124 (85.5%)	101/106 (95.3%)	393 $\pm$ 11	238 $\pm$ 20
	83	152/153 (99.3%)	87/89 (97.6%)	511 $\pm$ 33	520 $\pm$ 23
	98	25/31 (80.6%)	67/72 (93.1%)	408 $\pm$ 64	158 $\pm$ 23
12–24w	124	29/42 (69.0%)	75/80 (93.8%)	391 $\pm$ 45	231 $\pm$ 28
	153	93/109 (85.3%)	109/110 (99.1%)	380 $\pm$ 31	443 $\pm$ 37
	190	117/130 (90.0%)	108/108 (100.0%)	308 $\pm$ 19	286 $\pm$ 24

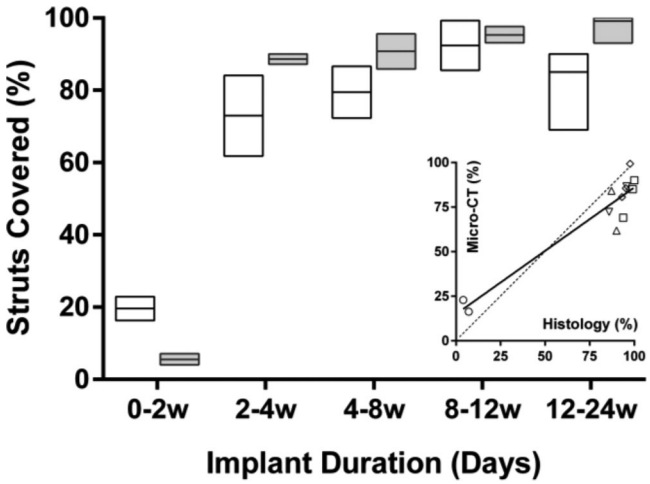

Fig. 3. Percentage of stent struts covered in neointima assessed by micro-CT (clear bars) and histology (gray bars), showing a significant increase in percentage of struts covered at implant durations greater than 2 weeks (0–2w). The percentage of struts covered was observed to remain relatively stable and greater than 60% after 2 weeks for implant durations of between 2 and 4 weeks (2–4w), 4 to 8 weeks (4–8w), 8 to 12 weeks (8–12w), and 12 to 24 weeks (12–24w). Bars indicate median $\pm$ range. (Inset) Animal specific comparison of the percentage of struts covered between micro-CT images and histological sections for 0–2w (circles), 2–4w (up-triangles), 4–8w (down-triangles), 8–12w (diamonds), and 12–24w (squares). For animals implanted less than 2 weeks, a larger percentage of incorporated struts were observed from micro-CT imaging, with a larger percentage of incorporated stent struts observed from histological sections at implant durations greater than 2 weeks. Dotted line indicates unity, with solid line indicative of regression fit with a slope of 0.71 $\pm$ 0.08 ($R^2 = 0.8903$).

the average percentage of incorporated stent struts increased from 19.0 $\pm$ 4.6% (mean $\pm$ SD, $n = 2$ animals, $n = 84$ struts) within the initial 2 weeks to 72.4 $\pm$ 15.7% (mean $\pm$ SD, $n = 2$ animals, $n = 145$ struts) between 2 and 4 weeks. Similarly, we observed a significant increase in the histologically determined percentage of incorporated stent struts after a two-week implantation period, increasing from 5.43 $\pm$ 2.2% (mean $\pm$ SD, $n = 2$ animals, $n = 184$ struts) within the first 2 weeks to 87.8 $\pm$ 2.0% (mean $\pm$ SD, $n = 2$ animals, $n = 98$ struts) between 2 and 4 weeks. A four-parameter dose–response curve was fit to the micro-CT and histologically assessed percentage of stent struts covered in neointima using GraphPad Prism (6.05, GraphPad Software, Inc., USA), and indicated more than 84% of the struts would be covered after 14 days (adjusted R^2 of 0.9973 and 0.9999 for micro-CT and histology, respectively). There was statistically significant correlation between micro-CT and histological assessment, with a Pearson coefficient of 0.9436, ($R^2 = 0.8903$, $P < 0.0001$). In both animals implanted for less than 2 weeks, there was a larger percentage of observed struts covered when images were assessed using micro-CT as compared with histological sections (Fig. 3 Inset). For almost all other animals implanted for greater than 2 weeks, histological evaluation returned a higher observed percentage of covered struts than micro-CT evaluation.

B. Strut-to-Lumen Distance

Strut-to-lumen distances were calculated for the ten animals that were implanted for durations longer than 2 weeks (see Table I, Fig. 4). The two animals implanted for zero and nine days were not evaluated due to the small number of incorporated stent struts (4–8). An initial decrease in neointimal thickness (strut-to-lumen distance) was observed from micro-CT assessed images in the first month after implantation, decreasing from $570 \pm 33\,\mu$m (mean $\pm$ SD, $n = 105$ struts) 2 to 4 weeks following implantation to $367 \pm 10\,\mu$m (mean $\pm$ SD, $n = 257$ struts) between 4 and 8 weeks. Strut-to-lumen thickness was observed to stabilize thereafter. There was a minor time-dependent alteration in neointimal thickness observed from samples assessed using histological methods, with the average strut-to-lumen distance of $254 \pm 26\,\mu$m (mean $\pm$ SD, $n = 86$ struts) measured between 2 and 4 weeks, increasing to $331 \pm 19\,\mu$m (mean $\pm$ SD, $n = 292$ struts) for animals implanted for longer than 12 weeks. For measurements of neointimal thickness, there was no correlation between micro-CT and histology (Pearson coefficient $= 0.2911$, $R^2 = 0.0847$, $P = 0.4144$) and in almost all samples, there was an expected overestimation of the strut-to-lumen distance measured using micro-CT images, corresponding with the origin of the micro-CT measurements being centroid (see Fig. 4 inset).

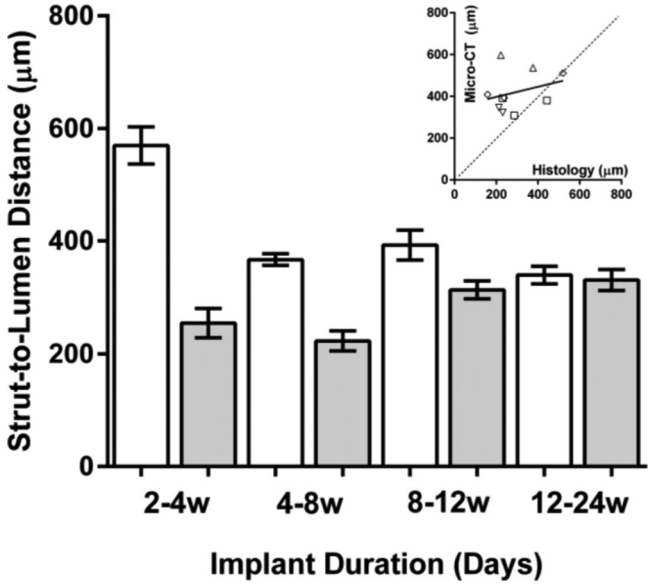

Fig. 4. Average strut-to-lumen distance measured from micro-CT images (clear bars) and histological sections (gray bars) showing median (± SEM) for animal subsets implanted for 2 to 4 (2–4w), 4 to 8 (4–8w), 8 to 12 (8–12w), and 12 to 24 (12–24w) weeks. There was a decrease in neointimal thickness as a function of time for micro-CT measurements, with a slight increase (254 ± 26 μm to 330 ± 19 μm) observed from histological sections between 2–4w and 12–24w. (Inset) Animal specific comparison of strut-to-lumen distances obtained from ten animals implanted with a Stentrode in the superior sagittal sinus for up to 190 days showing average and standard deviation of strut-to-lumen distances for 2–4w (up-triangles), 4–8w (down-triangles), 8–12w (diamonds), and 12–24w (squares). Dotted line is indicative of unity, with most data points showing larger strut-to-lumen distances measured from micro-CT images. Solid line is indicative of linear regression with a slope of 0.242 ± 0.28. $R^2 = 0.7409$.

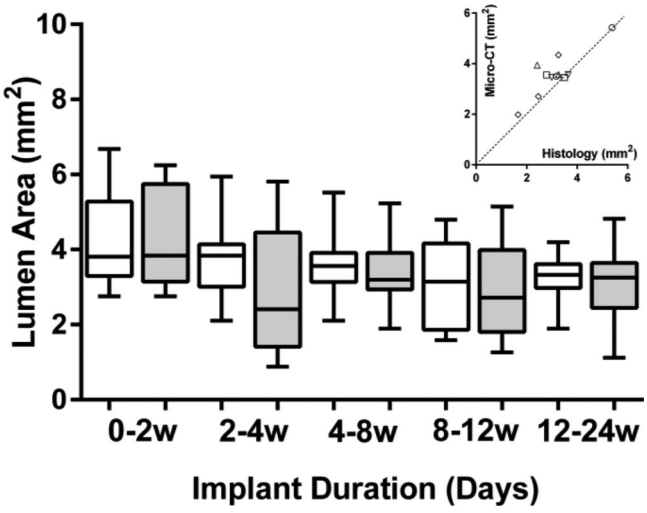

Fig. 5. Lumen area measured from micro-CT images (clear bars) and histological sections (gray bars), showing median ± SEM and range for animal subsets implanted for 2 to 4 (2–4w) weeks, 4 to 8 weeks (4–8w), 8 to 12 weeks (8–12w), and 12 to 24 weeks (12–24w). There was no observation of vascular occlusion from any image or section from any animal. (Inset) Animal specific comparison between micro-CT and histological assessed vessel areas for 0–2w (circles), 2–4w (up-triangles), 4–8w (down-triangles), 8–12w (diamonds), and 12–24w (squares). Dotted line indicates unity, with solid line a regression fit to the data (slope = 0.79 ± 0.16, $R^2 = 0.7264$).

C. Lumen Area

Lumen areas were also measured using micro-CT and histopathology to assess whether implantation of a Stentrode within the superior sagittal sinus would cause vascular occlusion. All 12 animals implanted with a device for up to 190 days were observed to have patent vessels (see Fig. 5). In three nonimplanted controls, the micro-CT measured lumen area was 5.48 ± 0.78 (mean ± SD, $n = 3$ animals, $n = 65$ sections). For animals implanted with a device for less than 2 weeks, the observed lumen area was slightly reduced to $4.28 \pm 0.17\,\mathrm{mm}^2$ (mean ± SEM, $n = 49$ sampled images). This remained relatively stable across animals implanted for 2 to 4 weeks ($3.75 \pm 0.13\,\mathrm{mm}^2$, $n = 40$), 4 to 8 weeks ($3.51 \pm 0.10\,\mathrm{mm}^2$, $n = 46$), 8 to 12 weeks ($3.10 \pm 0.14\,\mathrm{mm}^2$, $n = 63$) and for greater than 12 weeks ($3.27 \pm 0.06\,\mathrm{mm}^2$, $n = 60$). The mean lumen area, when assessed via measurements of using histopathological sections, was observed to decrease from a less-than-two week area of $4.32 \pm 0.25\,\mathrm{mm}^2$ (mean ± SEM, $n = 25$ sections) to $2.86 \pm 0.32\,\mathrm{mm}^2$ ($n = 25$), $3.39 \pm 0.16\,\mathrm{mm}^2$ ($n = 21$), $2.78 \pm 0.21\,\mathrm{mm}^2$ ($n = 27$) and $3.06 \pm 0.14\,\mathrm{mm}^2$ ($n = 26$) after 2 to 4, 4 to 8, 8 to 12, and greater than 12 weeks, respectively. There was a strong correlation between the lumen diameters measured using micro-CT and histology, with a Pearson coefficient of 0.8523 ($R^2 = 0.7264$, $P = 0.0009$).

D. Lumen-to-Electrode Distance

Electrode-to-lumen distances were only measured using histological techniques, due to large blooming artifacts observed around the electrodes when imaged using micro-CT [see Fig. 2(F)]. There was an increase in the electrode-to-lumen distance as a function of time (see Fig. 6), increasing from 0 ± 0 μm (mean ± SD, $n = 5$ electrodes) to 94 μm ($n = 1$ electrode) after implantation duration of 2 to 4 weeks and to 228 ± 67 μm (mean ± SD, $n = 5$ electrodes), 167 ± 45 μm (mean ± SEM, $n = 7$ electrodes) and 460 ± 92 (mean ± SD, $n = 8$ electrodes) for durations of four to eight, 8 to 12 and 12 to 24 weeks, respectively. There was no correlation between strut-to-lumen distance and electrode-to-lumen distance (see Fig. 7 inset), with most electrodes having a smaller neointimal thickness than the measured strut-to-lumen distance of the stent struts, presumably to the presence of the glue that was not included in measurements of thickness.

IV. Discussion

A comparison was made between the number of stent struts completely covered in neointima in sheep implanted with a Stentrode in the superior sagittal sinus, for up to 190 days, using synchrotron-acquired micro-CT images and photographs of histological sections.

The percentage of stent struts covered in neointima increased significantly for 2 weeks following implantation. 5.43% (10/184) of struts were observed by histology to be incorporated in devices implanted for less than 2 weeks, increasing to 87.8% (86/98) for devices implanted between 2 and 4 weeks. While the 50–70 μm struts measured by micro-CT were affected by

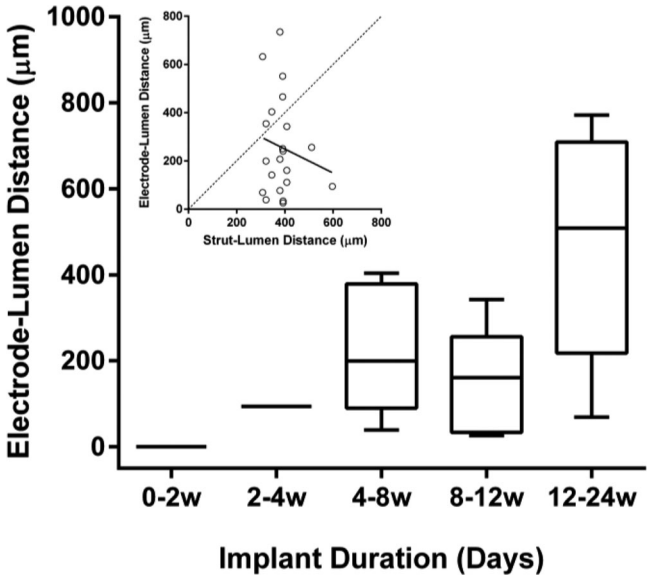

Fig. 6. Neointimal thickness measured as the distance between an implanted electrode and the internal lumen for animals implanted for up to 24 weeks. No electrodes were completely covered in neointima when implanted for up to 2 weeks ($n = 5$ electrodes). (Inset) Comparison between electrode-to-lumen distance and strut-to-lumen distance for all animals implanted. Dotted line indicates unity, with solid line indicative of a linear regression fit to the data (slope $= -0.49$, $R^2 = 0.0268$).

a blooming artifact, resulting in classification of struts with 0–10 μm of intimal tissue as uncovered, there was a strong correlation between both modalities (Pearson coefficient of 0.9436, $R^2 = 0.8903$, $P < 0.0001$). There was also an increase in incorporation from 19.0% (16/84) prior to 2 weeks to 72.4% (105/145) for micro-CT evaluated devices implanted for between 2 and 4 weeks. This strongly supports the safety of stenting the superior sagittal sinus, with >70% of struts covered with neointima representing a decreased risk of thrombosis in coronary stenting [14]. One month after implantation, 87.3% (627/718) and 95.5% (701/734) of stent struts were identified as incorporated, as assessed by micro-CT and histology, respectively. This has implications for the necessary duration of antiplatelet agents, such as aspirin or clopidogrel, required to prevent or reduce the potential of thrombosis. As the first histological study of a cerebral venous sinus stent, this provides an insight as to the differences between the rate of neointimal proliferation between cerebral venous and coronary arterial stents. We observed that strut incorporation was stable for 2 weeks after implantation, which is comparable to reports of coronary arterial stent incorporation, plateauing between 2 weeks and four months [18], [31].

Strut-to-lumen distances for all animals implanted for greater than 4 weeks was $300 \pm 10\,\mu$m (mean $\pm$ SEM, $n = 690$ struts) for histology and $365 \pm 12\,\mu$m (mean $\pm$ SEM, $n = 619$ struts) for micro-CT. Micro-CT assessed images recorded larger neointimal thicknesses as they were measured from center of the strut to the lumen edge due. Taking into account a reported strut diameter of 50–70 μm [25], the neointimal thickness is reduced to 330 μm, and is in close agreement with histological assessment. Furthermore, processing and embedding causes tissue shrinkage of up to 20% [32], which may distort the tissue architecture around the rigid stent struts, causing a reduction in the measured neointimal thickness. The thickness of neointima over the struts, assessed using either modality, was not uniform among devices and did not follow a temporal pattern. As the vessel increases in diameter along the anterio-posterior direction towards the confluence of sinus [11], the nonuniformity in strut–to-lumen distance is predicted to be caused by differences in the deposition location of the stents struts and microlocal factors such as inflammation [33], device deployment, and individual strut pressure on the vessel wall [34], [35].

Using histological sections, we also measured the thickness of neointima covering electrodes implanted for greater than 4 weeks. All 21 electrodes assessed were covered in neointimal tissue, with an average electrode-to-lumen distance of $256 \pm 204\,\mu$m (mean $\pm$ SD, $n = 21$). Our 50-μm-thick electrodes were attached to a 25 μm wire and covered with a thin layer of adhesive. As such, the thickness of the neointima from the side of the electrode facing the vessel wall to the lumen is around 330 μm. This is comparable to neointimal thickness of the stent struts, which can be summed as the thickness of the strut and the strut-to-lumen distance, which, averaged from all animals implanted for greater than 2 weeks is $296 \pm 273\,\mu$m (mean $\pm$ SD, $n = 776$).

There was a strong correlation ($p < 0.001$) between measurements of lumen area assessed by micro-CT and histology. While the lumen area decreased slightly over the 190 day implantation period from 4.29 ± 0.17 to $3.28 \pm 0.06\,\mathrm{mm}^2$ for micro-CT, (4.32 ± 0.25 to $3.06 \pm 0.17\,\mathrm{mm}^2$ measured from histopathological sections), there was no observation of vascular occlusion from any histological section or micro-CT image from any of the 12 animals implanted for up to 190 days. While this is not a direct measure of safety, this strongly suggests that a neural recording device, such as the Stentrode, can be implanted and tolerated chronically in the superior sagittal sinus.

Due to blooming artifacts that surrounded the large, 750-μm-diameter platinum electrodes, histological techniques were required for accurate assessment of electrode incorporation. Micro-CT, however, is a nondestructive alternative that enables easy, high-resolution imaging of implanted devices and avoids tissue loss inherent when resin-embedded sections are cut using a saw or microtome. There was, however, a strong correlation between the two imaging modalities for measurements of strut incorporation, strut-to-lumen thickness and lumen area, indicating that either technique can be used to accurately assess intimal incorporation of cerebral vessels implanted with a stent.

V. Conclusion

We have developed methods to demonstrate that micro-CT imaging and histopathological sections can both be used to identify and interrogate neointimal proliferation occurring to stent-electrode array implanted chronically in the superior sagittal sinus of sheep. We have shown that the number of exposed struts decreases significantly and stabilizes after 2 weeks, with neointima covering >85% of stent struts one month after

implantation. We used both modalities to determine the strut-to-lumen distance, and using histology, we observed the thickness of neointima covering the implanted electrodes was comparable to stent struts. Based on this data, a human study utilizing venous stenting may consider using aspirin or clopidogrel for a minimum of one month. There was a strong correlation between both modalities used to assess our implanted electrode array, with neither technique observing vascular occlusion from any animal implanted for up to 190 days, suggestive that cerebral vessels can chronically tolerate the implantation of a Stentrode. This study demonstrates preliminary safety of a stent-electrode array which may facilitate technological advances in minimally invasive brain–computer interface's.

References

[1] L. R. Hochberg *et al.*, "Reach and grasp by people with tetraplegia using a neurally controlled robotic arm," *Nature*, vol. 485, pp. 372–375, 2012.

[2] M. J. Cook *et al.*, "Prediction of seizure likelihood with a long-term, implanted seizure advisory system in patients with drug-resistant epilepsy: A first-in-man study," *Lancet Neurol.*, vol. 12, pp. 563–571, 2013.

[3] W. H. Theodore and R. S. Fisher, "Brain stimulation for epilepsy," *Lancet Neurol.*, vol. 3, pp. 111–118, 2004.

[4] R. A. Miranda *et al.*, "DARPA-funded efforts in the development of novel brain–computer interface technologies," *J. Neurosci. Methods*, vol. 244, pp. 52–67, 2015.

[5] M. A. M. Freire *et al.*, "Comprehensive analysis of tissue preservation and recording quality from chronic multielectrode implants," *PLoS One*, vol. 6, Nov. 2011.

[6] G. C. McConnell *et al.*, "Implanted neural electrodes cause chronic, local inflammation that is correlated with local neurodegeneration," *J. Neural Eng.*, vol. 6, Oct. 2009, Art. no. 056003.

[7] A. Prasad *et al.*, "Comprehensive characterization and failure modes of tungsten microwire arrays in chronic neural implants," *J. Neural Eng.*, vol. 9, 2012, Art. no. 056015.

[8] T. D. Y. Kozai *et al.*, "Brain tissue responses to neural implants impact signal sensitivity and intervention strategies," *ACS Chemical Neurosci.*, vol. 6, pp. 48–67, 2015.

[9] T. Saxena *et al.*, "The impact of chronic blood–brain barrier breach on intracortical electrode function," *Biomaterials*, vol. 34, pp. 4703–4713, 2013.

[10] H. M. Hamer *et al.*, "Complications of invasive video-EEG monitoring with subdural grid electrodes," *Neurology*, vol. 58, pp. 97–103, Jan. 2002.

[11] T. J. Oxley *et al.*, "Minimally invasive endovascular stent-electrode array for high-fidelity, chronic recordings of cortical neural activity," *Nature Biotechnol.*, vol. 58, pp. 97–103, 2016.

[12] T. F. Lüscher *et al.*, "Drug-eluting stent and coronary thrombosis biological mechanisms and clinical implications," *Circulation*, vol. 115, pp. 1051–1058, 2007.

[13] R. S. Schwartz *et al.*, "Restenosis and the proportional neointimal response to coronary artery injury: Results in a porcine model," *J. Amer. College Cardiol.*, vol. 19, pp. 267–274, 1992.

[14] A. V. Finn *et al.*, "Pathological correlates of late drug-eluting stent thrombosis: Strut coverage as a marker of endothelialization," *Circulation*, vol. 115, pp. 2435–2441, 2007.

[15] G. D. Dangas *et al.*, "In-stent restenosis in the drug-eluting stent era," *J. Amer. College Cardiol.*, vol. 56, pp. 1897–1907, 2010.

[16] W. Zheng *et al.*, "Endothelialization and patency of RGD-functionalized vascular grafts in a rabbit carotid artery model," *Biomaterials*, vol. 33, pp. 2880–2891, 2012.

[17] F. G. Welt and C. Rogers, "Inflammation and restenosis in the stent era," *Arteriosclerosis, Thrombosis, Vascular Biol.*, vol. 22, pp. 1769–1776, 2002.

[18] A. Farb *et al.*, "Pathological mechanisms of fatal late coronary stent thrombosis in humans," *Circulation*, vol. 108, pp. 1701–1706, 2003.

[19] N. Gonzalo *et al.*, "Optical coherence tomography patterns of stent restenosis," *Amer. Heart J.*, vol. 158, pp. 284–293, 2009.

[20] I. Uurto *et al.*, "Muraglitazar-eluting bioabsorbable vascular stent inhibits neointimal hyperplasia in porcine iliac arteries," *J. Vascular Interventional Radiol.*, vol. 26, pp. 124–130, 2015.

[21] N. Ohara *et al.*, "Superior sagittal sinus dural arteriovenous fistulas treated by stent placement for an occluded sinus and transarterial embolization a case report," *Interventional Neuroradiol.*, vol. 18, pp. 333–340, 2012.

[22] K. C. Wright *et al.*, "Percutaneous endovascular stents: An experimental evaluation," *Radiology*, vol. 156, pp. 69–72, 1985.

[23] D. Maintz *et al.*, "64-slice multidetector coronary CT angiography: In vitro evaluation of 68 different stents," *Eur. Radiol.*, vol. 16, pp. 818–826, 2006.

[24] M. Lettau *et al.*, "Angiographic CT: In vitro comparison of different carotid artery stents using two different angiography systems," *J. Neuroradiol.*, vol. 40, pp. 348–354, 2013.

[25] F. Miteff *et al.*, "Mechanical thrombectomy with a self-expanding retrievable intracranial stent (Solitaire AB): Experience in 26 patients with acute cerebral artery occlusion," *Amer. J. Neuroradiol.*, vol. 32, pp. 1078–1081, 2011.

[26] B. D. Metscher, "MicroCT for comparative morphology: Simple staining methods allow high-contrast 3D imaging of diverse non-mineralized animal tissues," *BMC Physiol.*, vol. 9, p. 11, 2009.

[27] A. W. Stevenson *et al.*, "First experiments on the Australian Synchrotron Imaging and Medical beamline, including investigations of the effective source size in respect of X-ray imaging," *J. Synchrotron Radiation*, vol. 17, pp. 75–80, 2009.

[28] K. Nieman *et al.*, "Noninvasive angiographic evaluation of coronary stents with multi-slice spiral computed tomography," *Herz*, vol. 28, pp. 136–42, 2003.

[29] N. Malik *et al.*, "Intravascular stents: a new technique for tissue processing for histology, immunohistochemistry, and transmission electron microscopy," *Heart*, vol. 80, pp. 509–516, 1998.

[30] P. Rippstein *et al.*, "Comparison of processing and sectioning methodologies for arteries containing metallic stents," *J. Histochemistry Cytochemistry*, vol. 54, pp. 673–681, 2006.

[31] P. H. Grewe *et al.*, "Acute and chronic tissue response to coronary stent implantation: Pathologic findings in human specimen," *J. Amer. College Cardiol.*, vol. 35, pp. 157–163, 2000.

[32] R. C. Puffer *et al.*, "Venous sinus stenting for idiopathic intracranial hypertension: A review of the literature," *J. Neurointerventional Surg.*, vol. 5, pp. 483–486, 2012.

[33] R. Kornowski *et al.*, "In-stent restenosis: Contributions of inflammatory responses and arterial injury to neointimal hyperplasia," *J. Amer. College Cardiol.*, vol. 31, pp. 224–230, 1998.

[34] L. H. Timmins *et al.*, "Increased artery wall stress post-stenting leads to greater intimal thickening," *Laboratory Investigation*, vol. 91, pp. 955–967, 2011.

[35] S. Morlacchi *et al.*, "Hemodynamics and in-stent restenosis: Micro-CT images, histology, and computer simulations," *Ann. Biomed. Eng.*, vol. 39, pp. 2615–2626, 2011.

Authors', photographs and biographies not available at the time of publication.